

# Different nanostructures caused by competition of intra- and inter- $\beta$ -sheet interactions in hierarchical self-assembly of short peptides



Peng Zhou<sup>a</sup>, Li Deng<sup>a</sup>, Yanting Wang<sup>b,\*</sup>, Jian R. Lu<sup>c,\*</sup>, Hai Xu<sup>a,\*</sup>

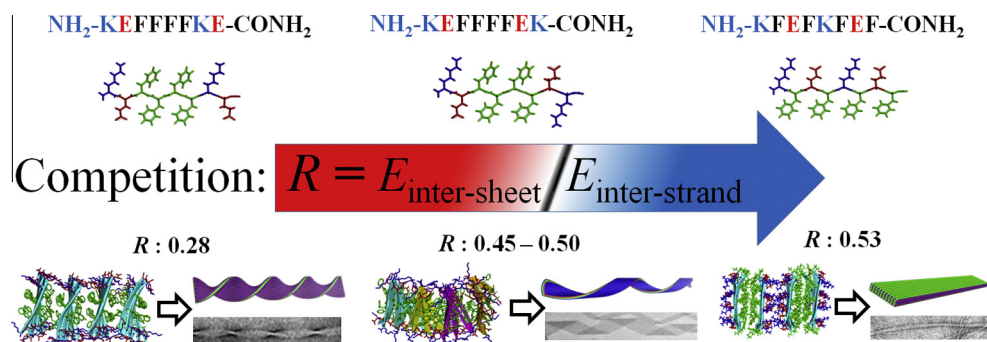
<sup>a</sup> State Key Laboratory of Heavy Oil Processing and Centre for Bioengineering and Biotechnology, China University of Petroleum (East China), 66 Changjiang West Road, Qingdao 266580, China

<sup>b</sup> State Key Laboratory of Theoretical Physics, Institute of Theoretical Physics, Chinese Academy of Sciences, 55 East Zhongguancun Road, P.O. Box 2735, Beijing 100190, China

<sup>c</sup> Biological Physics Group, School of Physics and Astronomy, The University of Manchester, Manchester M13 9PL, United Kingdom

## GRAPHICAL ABSTRACT

By tuning intra- and inter- $\beta$ -sheet interactions via peptide sequence variations and their competitions, different molecular packing modes are obtained and then grow into three typical nanostructures (twisted ribbons, helical ribbons/tubes and flat ribbons).



## ARTICLE INFO

### Article history:

Received 6 August 2015

Revised 12 November 2015

Accepted 13 November 2015

Available online 14 November 2015

### Keywords:

Short peptides

Self-assembly

Nanostructures

Intermolecular interactions

Molecular packing modes

Molecular dynamics

## ABSTRACT

To understand how molecular interactions lead to the self-assembly of twisted, helical and flat nanoribbons, we have compared the hierarchical self-assembly processes of three selected octapeptides with the same amino acid composition but different sequences by both experiments and molecular dynamics (MD) simulations. KE-F8 (NH<sub>2</sub>-KEFFFFKE-CONH<sub>2</sub>) and EK-F8 (NH<sub>2</sub>-KEFFFFEK-CONH<sub>2</sub>) have the same distribution of hydrophobic residues and only differ by swapping the positive and negative charged residues at their C-terminals, while KFE-8 (NH<sub>2</sub>-KFEFKFEF-CONH<sub>2</sub>) differs from KE-F8 and EK-F8 by having all hydrophobic and charged residues evenly distributed. MD simulations indicated that the competition between electrostatic and hydrophobic interactions at the molecular level results in different initial packing modes: KE-F8 monomers form completely matched anti-parallel  $\beta$ -sheets, EK-F8 monomers align with one residue shifting, and KFE-8 monomers pack  $\beta$ -sheets with two heterogeneous surfaces, consistent with previously suggested models. Driven by inter-strand and inter-sheet interactions, further growth of these molecular templates leads to larger oligomers with different twisting and stacking degrees, which are structurally consistent with the experimentally observed self-assembled morphologies. Further MD simulations showed that the competition between intra- $\beta$ -sheet and inter- $\beta$ -sheet interactions is responsible for the different twisting and stacking degrees of  $\beta$ -sheets and the subsequent formation of different nanostructures (twisted ribbons for KE-F8, helical ribbons/tubes for EK-F8 and flat

\* Corresponding authors.

E-mail addresses: [wangyt@tp.ac.cn](mailto:wangyt@tp.ac.cn) (Y. Wang), [j.lu@manchester.ac.uk](mailto:j.lu@manchester.ac.uk) (J.R. Lu), [xuh@upc.edu.cn](mailto:xuh@upc.edu.cn) (H. Xu).

ribbons for KFE-8). This study thus provided an important mechanistic insight into the fine tuning of molecular packing and interactions via peptide sequence variation leading to controllable self-assembly of twisted, helical and flat nanostructures.

© 2015 Published by Elsevier Inc.

## 1. Introduction

Design and synthesis of molecules that self-assemble into well-ordered nanostructures is particularly attractive for developing new functional nanomaterials. Natural evolution and selection over billions of years have produced many intriguing biomolecules, which can form intricate and functional entities through countless interactions of self-assembly, such as lipid bilayers and vesicles, DNA double helices, three dimensional (3D) polypeptides and proteins, ribosomes and photo-harvesting systems. To design and fabricate nanomaterials and nanodevices through biomimetic or bioinspired self-assembly, we must accumulate knowledge through studying simpler molecular structures, especially the mechanisms how the molecular interactions lead to different self-assembled nanostructures and functions. In contrast to large proteins and long polypeptides, short peptides offer many advantages, such as structural stability, the ease of synthesis, and the easy establishment of the structure–function relationship and rational interpretation of various interactions involved in self-assembly. Thus, extensive endeavour has been devoted to short peptides and their self-assembly [1–6].

Hydrogen bonding (H-bonding) between backbones plays an important role in peptide self-assembly through driving peptide monomers to pack longitudinally into  $\beta$ -sheets [7,8]. The interactions among the side chains of peptide molecules (inter- $\beta$ -sheet interactions) regulate lateral packing of  $\beta$ -sheets at a much slower rate than the fast growth along the H-bonding direction [9]. Because  $\beta$ -sheets naturally tend to twist as a result of the inherent chirality of amino acids, the lateral interactions must overcome the elastic penalty of untwisting  $\beta$ -sheets from their natural states during their lateral packing [9–11]. The final assembled morphologies are the result of these interactions and/or confinements and their interplay. The above hierarchical self-assembly process has been manifested by several research groups through designed short peptides such as Ac-QQRFQWQFEQQ-CONH<sub>2</sub> (P<sub>11</sub>-II) [10,11], C<sub>16</sub>H<sub>31</sub>OVEVE and C<sub>16</sub>H<sub>31</sub>OVVEE [9,12], Ac-I<sub>4</sub>K<sub>2</sub>-CONH<sub>2</sub> and Ac-KI<sub>4</sub>K-CONH<sub>2</sub> [13]. Aggeli et al. have proposed a mathematical model that describes  $\beta$ -sheet twisting and stacking and have estimated the geometrical parameters of P<sub>11</sub>-II ribbons [11]. In experimental studies, systematic variations in peptide sequence have been adopted as an effective strategy on controlling the self-assembly and self-assembled nanostructures of ionic-complementary peptides [14–17].

Although experimental methods have provided a wealth of structural and morphological information on peptide self-assembly, it is usually hard through them to directly follow the hierarchical self-assembly evolution or dynamics from the molecular level to the nanoscale, in particular, to account for non-covalent interactions between molecules and energies of different molecular alignments. As a complementary tool, molecular dynamics (MD) simulations have been proved to be powerful in resolving the otherwise inaccessible features of the sub-units that underpin the overall peptide self-assembly [18–25].

Based on the competition between electrostatic and hydrophobic interactions (within  $\beta$ -sheets), we here carefully selected a group of peptides with an identical amino acid composition and length but different sequences. Each molecule has a specific sequence aimed at a particular molecular packing mode or structural template and a subsequent hierarchical organization.

Experimental studies (TEM, AFM, FTIR, and CD) indicated that they self-assembled into different one dimensional (1D) self-assembled morphologies with  $\beta$ -sheet secondary structures, including twisted ribbons/fibrils, helical ribbons/tubes and flat ribbons. The peptides thus comprise an ideal model system to perform complementary MD simulation investigations, aiming at mechanistically interpreting and connecting these different 1D morphologies. The relationship among molecular structures, monomer packing modes within  $\beta$ -sheets, lateral stacking and twisting of  $\beta$ -sheets, and the final self-assembled nanostructures was evaluated in such a nice model set. Furthermore, the molecular origin of different monomer packing modes was also analysed, in particular, the contributions of other non-covalent interactions (e.g. hydrophobic and electrostatic interactions) in addition to the H-bonding and their interplay.

## 2. Experimental and computational section

### 2.1. Peptide synthesis

The peptides were synthesized on a commercial CEM Liberty microwave peptide synthesizer from the C-terminal to the N-terminal using the standard Fmoc solid-phase synthesis strategy. The detailed procedures have been described in our previous work [8,26,27]. The use of Rink-amide MBHA resin allowed the C-terminal amidation. Coupling reactions were performed with a mixture of HBTU/HOBt/DIEA, and deprotection reactions were done with a 20% (v/v) piperidine and 0.1 M HOBt in DMF solution. Cleavage from the resin and deprotection of the protecting groups on the side chains were performed concurrently with a mixture of TFA, triisopropylsilane, and H<sub>2</sub>O at a ratio of 95:2.5:2.5. Each cleavage mixture was filtered into a round-bottomed flask and rotary evaporated. The solution was poured into ice-cold ether for precipitation. The suspension was centrifuged for 10 min at 4 °C at a rate of 10,000 rpm. The bottom solid product was collected, copiously rinsed with ice-cold ether, and centrifuged at the same condition. The ice-cold ether procedure was repeated for at least 6 times. The final products were lyophilized for 4 days and then subjected to reverse-phase high performance liquid chromatography (HPLC) and analysed by mass spectrometry (Figs. S1 and S2), and the purities of the three peptides were better than 95%.

### 2.2. Sample preparation

The lyophilized peptides were directly dissolved in Millipore water with a minimal resistivity of 18.2 M $\Omega$  cm, to produce 3 mM peptide solutions. The solution pH was carefully adjusted to ~6.2 so that the glutamic acid (E) residues were deprotonated and the lysine (K) residues were protonated.

### 2.3. Fourier transform infrared spectroscopy (FTIR)

The samples for FTIR characterization were prepared by dissolving the deuterated chloride salt of the peptide in D<sub>2</sub>O. The preparation of the deuterated chloride salt of the peptide was done based on the method described by Lamm et al. [28]. The resultant optically clear solutions were aged at room temperature at least for 2 days. FTIR was performed in absorbance mode on a Nicolet 6700 FT-IR spectrometer equipped with a DGTS detector. Solutions of

peptides in D<sub>2</sub>O were sandwiched between two CaF<sub>2</sub> plate windows (spacer 0.1 mm). Spectra were recorded at room temperature from 4000 to 400 cm<sup>-1</sup>, and 64 scans were collected at a spectral resolution of 4 cm<sup>-1</sup>. The data were corrected by subtracting the absorption of the related substrates. The derivative analysis was performed by using the OMINC software (Ver. 3.0, Nicolet).

#### 2.4. Circular dichroism (CD)

CD spectra were recorded on a MOS-450 spectrometer (Biologic, France) in a 0.1 mm quartz cell. The wavelength range was 190–260 nm, the scanning speed was 30 nm/min, and the bandwidth was 0.5 nm. Each spectrum was the average of at least three runs. A solvent background was subtracted. The resultant CD signals are expressed as  $[\theta]$  (10<sup>3</sup> deg cm<sup>2</sup> dmol<sup>-1</sup>) versus wavelength.

#### 2.5. Negative-stain transmission electron microscopy (TEM)

For the electron microscopy experiments, a 300 mesh copper grid, covered with carbon-stabilized Formvar film, was placed in 35  $\mu$ L sample solution. After about 3 min, the peptide solution was removed with a filter paper, and the grid was negatively stained with 2% (v/v) uranyl acetate in water for another 3 min, with excess dye being removed with a filter paper. The samples were viewed with a JEOL JEM-2100 UHR electron microscope with an accelerating voltage of 200 kV.

#### 2.6. Cryogenic TEM (Cryo-TEM)

Samples were prepared in a controlled environment vitrification system (CEVS).  $\sim$ 5  $\mu$ L of peptide solution was dropped onto a TEM copper grid coated with a laced support film and then wiped away with two pieces of filter paper, resulting in a thin film suspended on the mesh holes. After  $\sim$ 3 s, the samples were quickly plunged into a reservoir of liquid ethane (cooled by the nitrogen) at  $-165$  °C. Then, the vitrified samples were stored in the liquid nitrogen before transferring to the cryogenic sample holder (Gatan 626) and examined on a JEOL JEM-1400 electron microscope at about  $-174$  °C with an accelerating voltage of 120 kV.

#### 2.7. Atomic force microscopy (AFM)

Samples were prepared for AFM by dropping 10  $\mu$ L of peptide solution onto freshly cleaved mica surface for a few seconds (within 30 s). The mica surface was rinsed extensively with water and dried gently with ultrapure nitrogen gas. To prevent impurity adsorption on the prepared surface, AFM imaging was performed immediately after all traces of solvent had disappeared. AFM measurements were performed with a Nanoscope IVa MultiMode AFM (Digital Instruments, Santa Barbara, CA) in tapping mode. Topographic and phase images were concurrently recorded under ambient conditions, at  $512 \times 512$  pixel resolution, integral and proportional gains of 0.2 and 0.3, respectively, and a scanning speed of 1.5 Hz.

#### 2.8. Implicit solvent MD

Implicit solvent MD calculations were performed using the GROMACS 4.5.5 software package [29]. Peptide interactions were modelled by the OPLS all-atom force field [30]. Solvent effects were taken into account by the GBSA implicit-solvent model [31]. Both the electrostatic interactions and Lennard-Jones interactions used a cutoff of 2 nm and a time step of 1 fs was used. All simulations were performed using the constant NVT ensemble. The system temperature was initially set to 10 K and then increased to 203 K. After 500 ps equilibration, the temperature was raised to

293 K and kept constant for at least 1 ns using the Berendsen thermostat [32] with a time constant of 0.1 ps.

#### 2.9. Explicit solvent MD

Explicit solvent MD calculations were performed using the GROMACS 4.0.7 software package on the DeepComp7000 Super Computer. The peptide molecules were put in rectangular or cubic simulation boxes filled with water molecules. Periodic boundary conditions were applied to the simulation boxes. The OPLS all-atom force field and the tip4p water model were used in the simulations [30,33]. For all systems, to relax the initial configurations, the potential energy of the system was minimized by using the steepest-descent method until it converged. The solvent was then relaxed for 50 ps at 300 K, with the positions of the peptide atoms restrained by a harmonic potential. Bond lengths were constrained by the LINCS algorithm [34]. The electrostatic interactions were calculated using the Particle Mesh Ewald algorithm with a cutoff of 1.4 nm [35]. The cutoff radius for the Lennard-Jones interactions was set to 1.4 nm. A dielectric constant of 1 and a time step of 2 fs were used. All simulations were performed using the constant NPT ensemble. The temperature of the system was kept constant at 300 K using the Nosé–Hoover thermostat [36] with a time constant of 0.1 ps. The density of the system was adjusted according to the first constant NPT equilibration runs. The Parrinello–Rahman Method with the coupling time  $t_p = 0.5$  ps was used to implement the barostat with the pressure of  $P_0 = 1$  bar [37–39]. The trajectories were visually checked by using the GROMACS and VMD routines [40] to assess the quality of simulation. Pictures were generated by VMD and Accelrys Discovery Studio Visualizer [41]. Both solvent accessible surface area (SASA) and apolar surface area (APSA) of monomers and oligomers were calculated with a solvent probe radius of 0.14 nm. The main-chain inter-strand H-bonds were defined as donor–acceptor distance shorter than 0.35 nm and bond angle smaller than 30°. For the twisting angle calculation, the C $_{\alpha}$  atoms of the second and seventh residue were chosen to define the orientation of one peptide strand (Fig. S20). The inter-strand and inter-sheet non-bonded interactions were calculated with the sum of the van der Waals term and the coulomb term between all atom pairs in a cutoff of 1.4 nm.

### 3. Model molecules

As shown in Table 1, the selected three 8-residue peptides (denoted as KE-F8, EK-F8 and KFE-8, respectively) have an identical amino acid composition but different sequences. Reversed-phase HPLC analyses indicated their similar hydrophobicity (Table 1 and Fig. S1).

Due to its high hydrophobicity and strong  $\beta$ -sheet forming propensity, phenylalanine (F) residue plays a crucial role in amyloid fibrillogenesis [42,43]. Both KE-F8 and EK-F8 have four consecutive F residues at positions 3, 4, 5 and 6, thus generating a hydrophobic core in the middle and making them look like bola-amphiphiles. KE-F8 sequence is expected to produce a completely matched anti-parallel  $\beta$ -sheet packing, i.e. a zero-residue shift [17], which means that all molecules within the formed  $\beta$ -sheet are anticipated to have their four hydrophobic F residues perfectly aligned and the other four charged residues form salt bridge bonds with the oppositely charged residues of neighbouring molecules. On the other hand, EK-F8 has symmetric amino acids along the sequence, whose only difference from KE-F8 is the swapping of the E and K residues at its C-terminus. This design may lead to a competition between the hydrophobic and electrostatic interactions within  $\beta$ -sheets. The charge complementarity between EK-F8 molecules is expected to cause residue shifting between the

**Table 1**  
Sequence and hydrophobicity of the model peptides.

Peptide	Sequence <sup>a</sup>	HPLC retention time (min) <sup>b</sup>	SASA (nm <sup>2</sup> ) <sup>c</sup>	APSA (nm <sup>2</sup> ) <sup>c</sup>
KE-F8	NH <sub>3</sub> <sup>+</sup> -K <sup>+</sup> E <sup>-</sup> FFFFK <sup>+</sup> E <sup>-</sup> -CONH <sub>2</sub>	16.8	13.6 ± 0.1	8.00 ± 0.05
EK-F8	NH <sub>3</sub> <sup>+</sup> -K <sup>+</sup> E <sup>-</sup> FFFFE <sup>-</sup> K <sup>+</sup> -CONH <sub>2</sub>	16.9	13.5 ± 0.1	7.98 ± 0.05
KFE-8	NH <sub>3</sub> <sup>+</sup> -K <sup>+</sup> FE <sup>-</sup> FK <sup>+</sup> FE <sup>-</sup> F-CONH <sub>2</sub>	17.6	13.6 ± 0.1	7.99 ± 0.05

<sup>a</sup> Protonated K residues and the N-terminal amine group are marked in blue and deprotonated E residues in red.

<sup>b</sup> See HPLC profiles in Fig. S1 for details.

<sup>c</sup> Both solvent accessible surface area (SASA) and apolar surface area (APSA) were calculated based on the conformations sampled in our all-atom MD simulations. More details are given in the computational methods section.

neighbouring strands upon packing into a  $\beta$ -sheet, accompanied by decreased hydrophobic contact of the F residues. Without any residue shifting that means the four hydrophobic residues are fully matched, the neighbouring EK-F8 molecules would have direct electrostatic repulsions between the 4 pairs of charged residues, either in a parallel or anti-parallel arrangement.

As a traditional ionic-complementary peptide, KFE-8 has alternating hydrophobic and hydrophilic residues along the sequence. Similar to EK-F8, the molecules are supposed to have one-residue shift to allow the formation of either charge complementarity or complete hydrophobic collapse between strands when packing into  $\beta$ -sheets. Furthermore, due to the alternating distribution of hydrophobic/hydrophilic residues, a hydrophobic surface is expected to be exposed on one side of the formed  $\beta$ -sheet and a hydrophilic surface on the other side [14–18].

In comparison with Ac-KEFFFFKE-CONH<sub>2</sub> reported by the Nilsson group [17], KE-F8 is unblocked at its N-terminal, which results in a net positive charge around neutral pH and thus enhances its solubility and  $\beta$ -sheet-forming propensity [44]. For the same reason, all the three model peptides are unblocked at their N-terminals. In addition, KFE-8 has two amino groups near its N-terminal while the widely studied Ac-FKFEFKFE-CONH<sub>2</sub> has no charged group near its N-terminal [14,18,45].

Overall, the three model peptides have similar hydrophobicity and the same net charge. The rationale for selecting the three peptides is based on the rational usage of electrostatics and hydrophobic interactions. They are expected to produce different packing modes and specific assembling units, which in turn affect their self-assembled hierarchical structures.

## 4. Results and discussion

### 4.1. Self-assembled nanostructures by experiments

The FTIR measurements of the solutions of these peptides around neutral pH displayed two major peaks around 1620 and 1684 cm<sup>-1</sup>, characteristic of anti-parallel  $\beta$ -sheet secondary structures (Fig. S3) [17,42,46]. The CD spectrum of KFE-8 exhibited a maximum around 196 nm and a minimum around 217 nm, characteristic of  $\beta$ -sheet conformations (Fig. S4). However, the CD spectra of KE-F8 and EK-F8 displayed a positive peak around 207 nm rather than the above two  $\beta$ -sheet peaks. Such unusual CD signals have been observed in the self-assembly of Ac-KEFFFFKE-CONH<sub>2</sub>, whose FTIR spectrum also showed  $\beta$ -sheet structuring, and are likely to be related to aromatic  $\pi$ - $\pi$  effect [17]. However, the detailed mechanism is not clear. Negative-stain TEM, cryo-TEM and AFM imaging revealed that these peptides self-assembled into distinct 1D nanostructures manifested by different sizes, shapes and twisting (Figs. 1–3 and S5–S15).

#### 4.1.1. KE-F8

After 2 days of incubation, KE-F8 self-assembled into twisted ribbons, with widths in the range of 17–25 nm (Fig. 1A and D)

and thicknesses of around 3.3 nm (Fig. S5), close to the molecular length in the fully extended conformation. These twisted ribbons were micrometres in length and had pitches ranging from 30 to 140 nm, similar to those formed by Ac-KEFFFFKE-CONH<sub>2</sub> at pH 3–4 [17]. After 2 weeks, these long ribbons became wider with widths of 25–34 nm and pitches of 140–200 nm, but their thicknesses changed little (Fig. 1B). Note that some wider ribbons appeared to undergo a twisted-to-helical transition (yellow<sup>1</sup> arrow) which was also observed at the ends of some narrower ribbons (blue arrow). The thinner, twisted ribbons have a negative Gaussian, saddle-like curvature and are usually regarded as the precursors of the helical ribbons with cylindrical curvature [47,48]. In this case, we observed the coexistence of twisted and helical ribbons (even for several months of incubation). Although the helical ribbons could be regarded as partially healed nanotubes, no nanotubes were observed here, similar to the self-assembly of some peptide amphiphiles reported by Stupp and co-workers [49,50]. This was supported by cryo-TEM imaging (Fig. 1C).

#### 4.1.2. EK-F8

For EK-F8, no long nanostructures were observed from TEM characterization during the first 2 weeks. Instead, the self-assembled nanostructures were small and tile-like (Figs. 2A and S6). The edges of these peptide tiles were often observed to be tilted. This might be attributed to either their intrinsic twisting or the drying effect during specimen preparation. Measurements on the edges of these tilted tiles revealed that they had thicknesses around 3.7 nm (red arrows in Fig. 2A), which are a little bit larger than the fully extended molecular length of EK-F8. Note that the tilted edges could also be observed in AFM imaging (Fig. S7). After 1 month of incubation, we observed many long and helical ribbons with widths above 50 nm (Fig. 2D and Figs. S8 and S9) and importantly, nanotubes were formed (Fig. 2B and C). It can be seen from Fig. 2B that clear helical markings were still visible on the surface of a healed nanotube, and the width of its constituted ribbon was significantly increased, with a measured value around 391 nm. Nanotubes can be formed as the widths of the helical ribbons increase. In this mode of growth, the helical pitch remains constant and the ribbon gradually widens until the tube is healed or closed [47,51]. Their tubular nature was also verified by the clear dark edge lines in the cryo-TEM image (Fig. 2C, purple arrows). With prolonging incubation time to several months, many nanotubes were observed (Fig. S10).

#### 4.1.3. KFE-8

The main structural feature of the KFE-8 self-assembly was the formation of long filaments. Within the first 2 days of incubation, very thin protofilaments formed with widths of around 3.5 nm, close to the fully extended molecular length of KFE-8 (Fig. 3A). Their thicknesses were about 2.3 nm, close to the expected thickness (2.5 nm) of the bilayer with fully extended

<sup>1</sup> For interpretation of colour in Figs. 1 and 2, the reader is referred to the web version of this article.



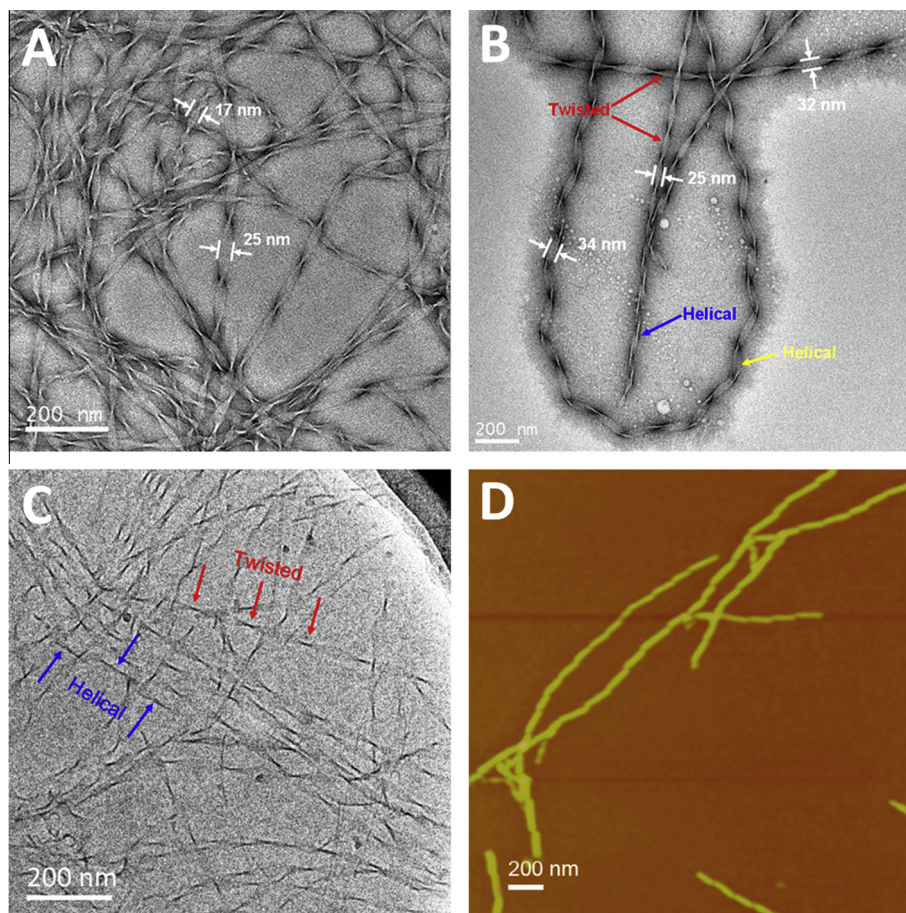


**Fig. 1.** Self-assembled nanostructures formed by KE-F8 (3 mM) in neutral solution. (A and B) Negative-stain TEM images after 2 days and 2 weeks of incubation. (C) Cryo-TEM image after 2 weeks of incubation. (D) AFM image after 2 days of incubation.

side chains (Fig. S11). Note from Fig. 3A that these protofilaments are already very long. After 1 week, there was a clear trend of the lateral attraction of parallel protofilaments into larger widths (Figs. S12 and S13). After 2 weeks, relatively smooth ribbons with widths of 10–50 nm and thicknesses of around 3.5 nm were observed (Figs. 3B and S14) and at this stage, the lateral association of parallel filaments was still observed prior to the ribbons forming (Inset of Fig. 3B). The flat nanoribbon morphology was further confirmed by cryo-TEM and AFM imaging (Fig. 3C and D). Note that in the cryo-TEM image, some flat ribbons were observed as darker lines due to their significant tilting (the ribbon surfaces are approximately parallel to the electron beam direction). After longer incubation of several months, we observed flat ribbons with much larger widths (Fig. S15). Note that Ac-FKFEFKFE-CONH<sub>2</sub> self-assembled into super-helical ribbons at pH of 3.3 during the early stage, which then transformed into flat ribbons [18]. However, Bowerman et al. have reported that the Ac-FKFEFKFE-CONH<sub>2</sub> super-helical ribbons were stable at neutral pH [45]. It is likely that both the sequence variation and the N-terminal amino group are responsible for the morphological difference observed in the self-assembly of KFE-8 and Ac-FKFEFKFE-CONH<sub>2</sub>.

In addition, the observed long and “mature” peptide ribbons showed different twisting degrees. The KFE-8 ribbons were quite flat, in contrast to the twisted and helical ribbons formed from KE-F8 and EK-F8. To gain insight into these differences among the self-assembled nanostructures of the three peptides, particularly to link their molecular structures and self-assembly, we then performed MD studies.

## 4.2. Packing modes by simulations

As a complementary approach to experimental characterizations, MD simulations are capable of revealing the molecular packing modes within  $\beta$ -sheets and the subsequent organizations of  $\beta$ -sheets during the very early stage of self-assembly. The preliminary MD simulations with an implicit solvent were performed to evaluate small pre-formed  $\beta$ -sheet assemblies of oligomers. The non-bonded potential energy was calculated to quantify the inter-strand packing modes and the lipophilic surface analysis was adopted to quantify the inter-sheet packing modes. At this stage, trimers were chosen as the smallest assembling units to evaluate these microscopic arrangements with H-bond structuring. Possible inter-strand packing modes, including both anti-parallel and parallel arrangements are shown in column 1 of Tables S1–S3 (ESI), with brief descriptions in column 2. Non-bonded potential energies (column 3) were calculated for these microscopic structures and taken as the criteria for their stability.

Basically, the arrangements with lower energies were found to be always associated with the anti-parallel  $\beta$ -sheets rather than the parallel  $\beta$ -sheets, which is consistent with our secondary structure characterization by FTIR. The reason for this phenomenon is supposed to be that longer H-bond lengths and unsuitable NH–O angles tend to make the parallel  $\beta$ -sheets less stable.

### 4.2.1. Inter-strand packing modes

Potential energy analysis shows that the zero-residue shift arrangement (4C\_4H\_0sh\_antiP) of the KE-F8 trimer has the lowest non-bonded potential energy, while the one-residue shift produces

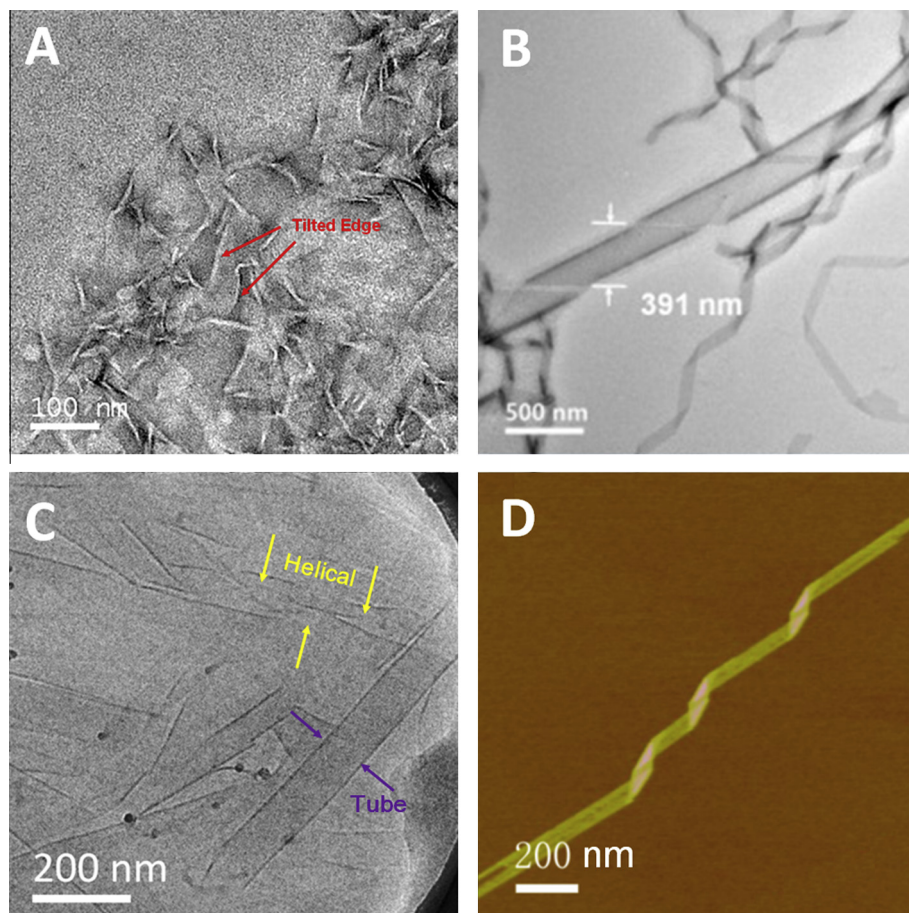


**Fig. 2.** Self-assembled nanostructures formed by EK-F8 (3 mM) in neutral solution. (A and B) Negative-stain TEM images after 2 weeks and 1 month of incubation. (C) Cryo-TEM image after 1 month of incubation. (D) AFM image after 1 month of incubation.

the lowest potential energies for both EK-F8 and KFE-8 trimers (Fig. 4B and Tables S1–S3). However, the EK-F8 trimer has four possible packing modes (2C\_3H\_1sh(I)\_antiP, 2C\_3H\_1sh(II)\_antiP, 2C\_3H\_1sh(III)\_antiP, and 2C\_3H\_1sh(IV)\_antiP), all with the lowest energies (Fig. 4B and Table S2). For the KFE-8 trimer, the 4C\_3H\_1sh\_antiP arrangement has the lowest energy (Fig. 4B and Table S3). The simulated monomer packing modes with the lowest energies agree with the rationale for selecting the three peptides.

#### 4.2.2. Inter-sheet arrangements

Sharing the same hydrophobic distribution, both KE-F8 and EK-F8  $\beta$ -sheets expose considerable hydrophobic surface regions in the direction perpendicular to the plane of the sheets, and thus tend to stack to reduce the exposed area of the hydrophobic surface to water. When we extended the assemblies from trimers to hexamers with the above six inter-strand packing modes with the lowest energies, the lipophilic surface analysis indicated the single sheets (6 strands) of KE-F8 or EK-F8 still remained stable (Fig. S16). In contrast, the KFE-8 hexamer sheet tended to bend and bury its hydrophobic face, forming a larger precursor of bilayers with a sharp increase of RPSA (relative polar surface area) during this structural transition (Fig. S16). The structural transition is ascribed to the presence of the two heterogeneous surfaces of the KFE-8 sheet, which favours the formation of stable bilayer segment *via* hydrophobic contact. These results imply that the basic assembling unit of KFE-8 is a bilayer. Note that, it does not mean that the homogeneous surface of KE-F8 and EK-F8 can make their single layers stable enough for large populations. When we further extended to 12-oligomers, stable bilayers (6 strands  $\times$  2 sheets)

were observed with decreasing non-bonded potentials (Fig. 4C). We expect that multi-layered oligomers will form with increasing populations for KE-F8 and EK-F8.

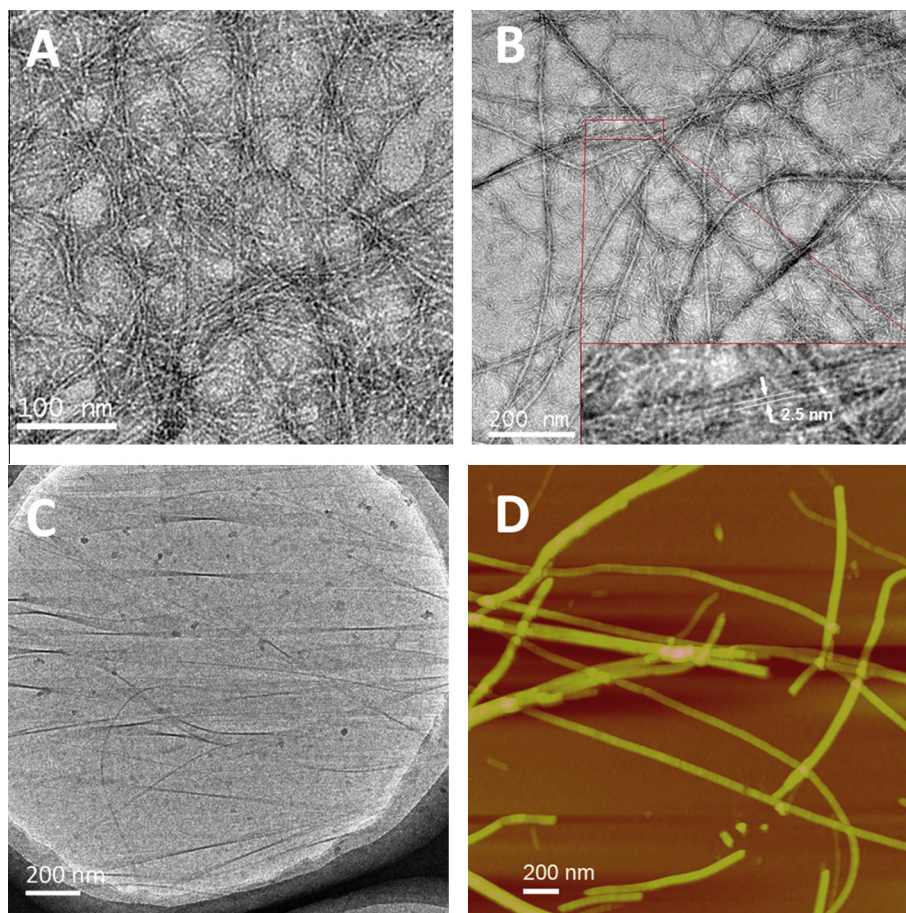
The above results from the preliminary MD calculations show that the distributions of positive/negative charged residues along the backbone determine the inter-strand arrangements, and the distributions of hydrophilic/hydrophobic residues along the sheets determine the nature of the contact between sheets.

#### 4.3. Further simulations and mechanism

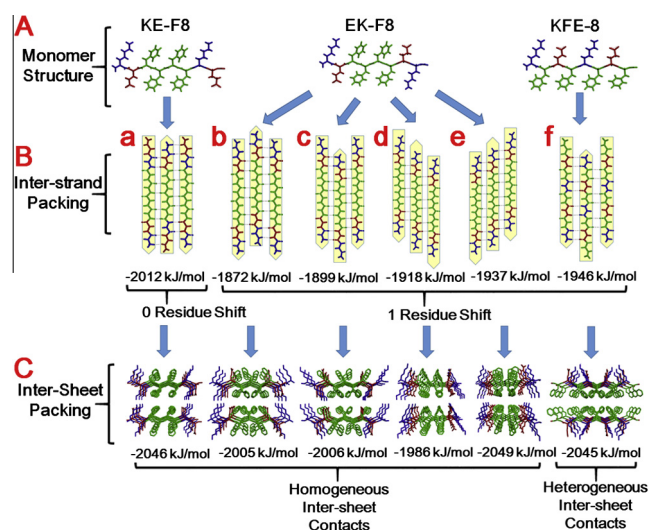
Based on the preliminary MD simulation and experimental investigations, we then performed MD simulations for further structural rationalization, by constructing assembled templates with enlarged oligomer sizes in two directions (from 6 strands  $\times$  2 sheets to 12 strands  $\times$  2 sheets and 6 strands  $\times$  4 sheets). In order to gain more reasonable structural information, the solvent was explicitly represented so that interactions between charged groups and polar solvent could be accurately calculated.

The peptide  $\beta$ -sheets were flat in the initial configurations of our simulation, but subsequently became twisted due to the intrinsic chirality of the constituent amino acid residues. In the case of 6 strands  $\times$  2 sheets, both the KE-F8 and EK-F8 sheets became progressively twisted as the simulation proceeded (Fig. S17A). The KE-F8 oligomer finished with the largest twisting angle of some 20° at the end of a 40-ns simulation. In contrast, the four  $\beta$ -sheet arrangements of EK-F8 showed smaller twisting angles of some 10°, 13°, 9° and 4°, respectively. For the KFE-8 oligomer, the twisting angle showed some oscillation but remained overall constant





**Fig. 3.** Self-assembled nanostructures formed by KFE-8 (3 mM) in neutral solution. (A and B) Negative-stain TEM images after 2 days and 2 weeks of incubation. (C) Cryo-TEM image after 2 weeks of incubation. (D) AFM image after 2 weeks of incubation. The inset of (B) shows the lateral association of parallel filaments into ribbons.

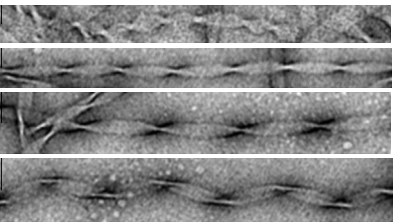
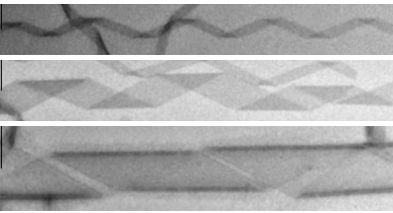
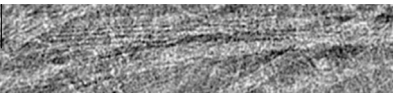


**Fig. 4.** Inter-strand and inter-sheet packing modes of the three model peptides. (A) Monomer structures. (B) Inter-strand packing modes and their non-bonded potential energy values (a: KE-F8-4C\_4H\_0sh\_antiP, b: EK-F8-2C\_3H\_1sh(I)\_antiP, c: EK-F8-2C\_3H\_1sh(II)\_antiP, d: EK-F8-2C\_3H\_1sh(III)\_antiP, e: EK-F8-2C\_3H\_1sh(IV)\_antiP, f: KFE-8-4C\_3H\_1sh\_antiP). 4C, 4H, 0sh, and antiP mean four charged residues forming salt-bridges, four hydrophobic residues in contact, no residue shift, and anti-parallel orientation, respectively. (C) Inter-sheet packing modes and their non-bonded potential energy values. Note that the KFE-8 bilayer has a pure and intense inter-sheet hydrophobic contact.

at some 5°. As shown in Fig. S17B and C, most of the simulated twisting angles became compromised when the oligomers were extended along the directions of sheet packing and H-bonding, except for the values of the two modes of EK-F8 (EK-F8-2C\_3H\_1sh(III)\_antiP and EK-F8-2C\_3H\_1sh(IV)\_antiP). For instance, the twisting angle was reduced to some 10° for KE-F8, some 5° and 10° for EK-F8-2C\_3H\_1sh(I)\_antiP and EK-F8-2C\_3H\_1sh(II)\_antiP, and some 2° for KFE-8, in the case of 6 strands  $\times$  4 sheets at the end of a 40-ns simulation. Furthermore, the simulated twisting angles were greater than those measured in experiment (Table 2), possibly due to a significant increase in width for the observed nanostructures relative to the simulated oligomers. In fact, the measured twisting angles for KE-F8 and EK-F8 showed a decreasing trend as the nanoribbons became wider (Table 2). Thus, the experimental data in this aspect can be regarded as the final result of simulation runs at larger space scale and longer time scale.

As indicated above, the intrinsic twisting of  $\beta$ -sheets is restrained by their lateral stacking. The topology of the self-assemblies is not only governed by inter- $\beta$ -sheet attractions but also inter- $\beta$ -strand (intra- $\beta$ -sheet) interactions based on the model sponsored by Selinger and coworkers [48]. The 6 strands  $\times$  4 sheets oligomers can be considered as a chiral elastic network, which is connected by intra- $\beta$ -sheet interactions along the long axis and inter- $\beta$ -sheet interactions along the lateral orientation (Fig. 5). As shown in Table 3, KE-F8 has a strong inter-strand connection ( $-642.0$  kJ/mol) due to the completely complementary charge interaction and the large hydrophobic surface contact (with a hydrophobic area loss of  $-4.20$  nm<sup>2</sup>). The inter-sheet attraction is

**Table 2**  
Measured twisting angles ( $\theta_{\text{twist}}$ ) of the nanostructures formed by KE-F8, EK-F8, and KFE-8.

Peptide	Morphology	Type	Width (nm)	$\theta_{\text{twist}}$ ( $^{\circ}$ ) <sup>a</sup>
KE-F8		Twisted ribbon	17 ± 2	2.94 ± 0.34
		Twisted ribbon	25 ± 2	0.63 ± 0.07
		Twisted ribbon	32 ± 2	0.45 ± 0.03
		Helical ribbon	34 ± 2	0.55 ± 0.02
EK-F8		Helical ribbon	52 ± 2	0.28 ± 0.03
		Helical ribbon	167 ± 12	0.20 ± 0.02
		Helical ribbon	391 ± 11	0.18 ± 0.02
KFE-8		Flat ribbon	20–50	0

<sup>a</sup> Here, the twisting angle ( $\theta_{\text{twist}}$ ) was experimentally determined from TEM imaging according to the methods described in Fig. S18.

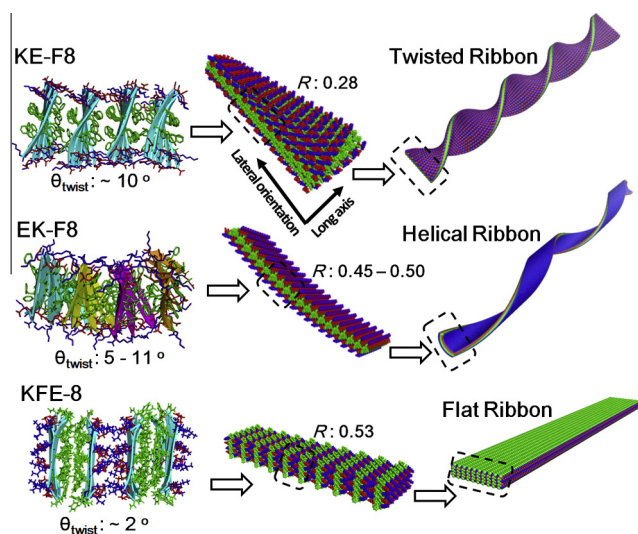


**Fig. 5.** Schematic illustration of the hierarchical self-assembly processes and the self-assembled topologies of the three model peptides. For KE-F8, oligomers (6 strands × 4 sheets) with fully matched  $\beta$ -sheets have twisting angles of  $\sim 10^{\circ}$  and an inter-sheet/intra-sheet interaction ratio  $R$  of 0.28 and eventually develop into twisted ribbon topology. For EK-F8, four kinds of  $\beta$ -sheets with one-residue shift (marked by four colours) have twisting angles ranging from  $5^{\circ}$  to  $11^{\circ}$  and a  $R$  value of 0.45–0.50 and eventually develop into helical ribbon topology. For KFE-8,  $\beta$ -sheets bilayers with one-residue shift have twisting angles smaller than  $2^{\circ}$ , and a  $R$  value of 0.53, and finally form flat ribbon topology.

attributed to both the inter-sheet interaction ( $-1064.8$  kJ/mol) and the inter-sheet hydrophobic surface area loss ( $-11.14$  nm<sup>2</sup>). Compared with KE-F8, EK-F8 has weaker inter-strand interactions ( $-439.7$  to  $-502.9$  kJ/mol) due to less charged side chains attraction. However, there are stronger inter-sheet interactions ( $-1522.4$  to  $-1222.0$  kJ/mol) in all four types of EK-F8 packing modes. This indicates more intense contacts among  $\beta$ -sheets and more hydrophobic surface buried in the assemblies ( $-12.60$  to  $-13.92$  nm<sup>2</sup>). The decreased inter-strand interactions and the increased inter-sheet interactions-work together to result in

helical ribbons with cylindrical curvature (Fig. 5). Meanwhile, the stronger inter-sheet interactions enhance the lateral packing and thus increase the width of the helical ribbons which eventually grow to nanotubes.

Similar to KE-F8, KFE-8 also has four pairs of matched charged residues but one less hydrophobic residue matched upon forming  $\beta$ -sheets. As a result, KFE-8 has a weaker inter-strand interaction than KE-F8 but stronger than EK-F8 (Table 3). One significant feature of the KFE-8 sheet is the formation of two distinct surfaces, and the strong hydrophobic interaction (with an extremely high hydrophobic loss of  $-17.85$  nm<sup>2</sup>) between the hydrophobic surfaces leads to the formation of bilayers as the basic assembling unit. The alternating distributions of positively and negatively charged residues on the two hydrophilic surfaces of a bilayer make the lateral adhesion interactions well-ordered and extremely strong among bilayers ( $-1656.5$  kJ/mol). Although  $\beta$ -sheets are not flat due to the intrinsic chirality of the constituted amino acids, the strong interactions between sheets restrict their twisting propensity and thus lead to rather flat nanoribbon morphology.

To better characterize the competition between the inter- $\beta$ -sheet and intra- $\beta$ -sheet interactions, we calculated the ratio  $R$  ( $E_{\text{inter-sheet}}/E_{\text{inter-strand}}$ ).  $E_{\text{inter-sheet}}$  is the interaction between molecules of adjacent  $\beta$ -sheets, which corresponds to the stretch elastic modulus in the model of Selinger et al. [48]. Its values were obtained as one sixth of the inter-sheet interaction from the MD simulations of 6 strands × 4 sheets oligomers (Table 3).  $E_{\text{inter-strand}}$  is the interaction between  $\beta$ -strands, which corresponds to the bend elastic modulus in the model of Selinger et al. [48].  $R_{\text{KE-F8}}$ ,  $R_{\text{EK-F8}}$ , and  $R_{\text{KFE-8}}$  were determined to be 0.28, 0.45–0.50, and 0.53, respectively. Higher  $R$  value represents stronger lateral packing and less twisting for the assembled nanostructures (Fig. 5).

Monitoring the number of inter-backbone H-bonds can provide accurate information for residue matching and inter-strand interaction in the  $\beta$ -sheet arrangement. In the case of 6 strands × 2 sheets, KE-F8 has more H-bonds than EK-F8 on average due to one-residue shift of the latter (Fig. S17D). In contrast, although there is also a one-residue shift in KFE-8, the flat nanostructure stabilizes H-bonding, resulting in more H-bonds than in EK-F8. As the twisting degree decreases in larger oligomers (12 strands × 2 or 6



**Table 3**Inter- $\beta$ -strand and inter- $\beta$ -sheet interactions and hydrophobic area losses of the 6 strands  $\times$  4 sheets oligomers.

Packing mode	Inter-strand interaction (kJ/mol)	Inter-sheet interaction (kJ/mol)	Inter-strand hydrophobic surface area loss (nm <sup>2</sup> )	Inter-sheet hydrophobic surface area loss (nm <sup>2</sup> )
a: KE-F8-4C_4H_0sh_antiP	−642.0 $\pm$ 34.0	−1064.8 $\pm$ 255.9	−4.20 $\pm$ 0.07	−11.14 $\pm$ 0.54
b: EK-F8-2C_3H_1sh(I)_antiP	−453.4 $\pm$ 44.1	−1234.3 $\pm$ 184.1	−3.99 $\pm$ 0.10	−12.60 $\pm$ 0.89
c: EK-F8-2C_3H_1sh(II)_antiP	−439.7 $\pm$ 30.3	−1222.0 $\pm$ 153.8	−3.43 $\pm$ 0.11	−13.92 $\pm$ 1.35
d: EK-F8-2C_3H_1sh(III)_antiP	−502.9 $\pm$ 45.0	−1522.4 $\pm$ 72.5	−4.00 $\pm$ 0.15	−13.73 $\pm$ 1.22
e: EK-F8-2C_3H_1sh(IV)_antiP	−479.3 $\pm$ 25.9	−1361.4 $\pm$ 290.5	−3.89 $\pm$ 0.15	−13.34 $\pm$ 1.65
f: KFE-8-4C_3H_1sh_antiP	−523.0 $\pm$ 19.6	−1656.5 $\pm$ 116.6/−460.2 $\pm$ 18.5 <sup>a</sup>	−3.64 $\pm$ 0.16	−2.30 $\pm$ 0.02/−17.85 $\pm$ 0.07 <sup>a</sup>

<sup>a</sup> KFE-8 has two types of inter-sheet contacts. The interface between hydrophilic surfaces has a strong electrostatic attraction but a weak hydrophobic effect, while the interface between hydrophobic surfaces bears a high surface area loss indicating a strong hydrophobic effect.

strands  $\times$  4 sheets), the average number of H-bonds between two strands tends to increase, as shown in Fig. S17E and F.

Inter-sheet packing was further analysed by monitoring the distances between sheets in the oligomers of 6 strands  $\times$  4 sheets. The distances were found to be uniform ( $\sim$ 1.3 nm) in the KE-F8 oligomers (Fig. S19A) after 40 ns of simulation, which is attributed to the similarity of contact types. KFE-8 has two distinct faces: the hydrophobic side-chain face which is compact ( $\sim$ 1.2 nm), and the charged side-chain face which is more open with some water molecules between them ( $\sim$ 1.4 nm), as shown in Fig. S19F. TEM characterization revealed a texture of KFE-8 nanoribbons that indicated clear separations of different interfaces. As shown in Fig. 3B, there are nanogrooves parallel to the nanoribbon long axis and the ridges (white lines) are  $\sim$ 2.5 nm in width, equivalent to the thickness of the peptide bilayer. For the four arrangements in EK-F8 oligomers, the simulated distances between sheets are slightly shorter than that in KE-F8 (Fig. S19B–E). This supports the conclusion that the lateral packing is more intense in EK-F8.

Note that for EK-F8, the four inter-strand packing modes have comparably identical energies as a result of the competition between electrostatic and hydrophobic interactions. This feature makes the peptide assemble into large quantities of short tiles at the early stage of self-assembly (Figs. 2A and S6).

## 5. Conclusions

By using a combination of computational and experimental methods, this work has demonstrated the relationship between molecular packing modes and the three types of self-assembled nanostructures (twisted, helical and flat nanoribbons), which have been widely found in peptide self-assembly by many researchers [13,17,47–50]. The results indicated that the competition between electrostatic and hydrophobic interactions affects the inter-strand packing modes and the competition between intra- $\beta$ -sheet and inter- $\beta$ -sheet interactions affects the twisting and stacking of  $\beta$ -sheets and the consequent mesoscopic structures. Along with evaluating the energy of different molecular alignments and the intermolecular interactions, molecular simulation techniques provided the vital details on the initial packing modes and structural characteristics, which can be correlated to the mesoscopic morphologies accessible to the experimental measurements.

The peptides considered here share the same amino acid composition, molecular weight and hydrophobicity, but have different molecular sequences to represent specific distributions of hydrophilic and hydrophobic properties along their molecular contours. Our present work demonstrated once again that peptide sequence variations are powerful in controlling self-assembling structures [13–17]. Furthermore, the similar hydrophobicity and the dominant role of electrostatic interactions in this model system made it suitable to compare the interactions within different molecular packing modes with  $\beta$ -sheet secondary structure. This work complemented the previous reported mechanisms and models of

peptide self-assembly [10,48]. It has also been shown that complementary information from molecular simulations and experimental results can help develop valuable insight into the early self-assembly stage and the subsequent structural organization of rationally designed peptides.

## Acknowledgements

This work was supported by the National Natural Science Foundation of China under grants Nos. 21373270 and 91227115. H.X. acknowledges the support by Program for New Century Excellent Talents in University (NCET-11-0735). J.R.L. thanks UK Engineering and Physical Sciences Research Council (EPSRC) and the Royal Society (London) for support. Allocations of computer time from the Supercomputing Centre in the Computer Network Information Centre at the Chinese Academy of Sciences are gratefully acknowledged.

## Appendix A. Supplementary material

Supplementary data associated with this article can be found, in the online version, at <http://dx.doi.org/10.1016/j.jcis.2015.11.030>.

## References

- [1] S. Zhang, *Nat. Biotechnol.* 21 (2003) 1171–1178.
- [2] R.V. Ulijn, A.M. Smith, *Chem. Soc. Rev.* 37 (2008) 664–675.
- [3] X. Yan, P. Zhu, J. Li, *Chem. Soc. Rev.* 39 (2010) 1877–1890.
- [4] X. Zhao, F. Pan, H. Xu, M. Yaseen, H. Shan, C.A.E. Hauser, S. Zhang, J.R. Lu, *Chem. Soc. Rev.* 39 (2010) 3480–3498.
- [5] H. Cui, M.J. Webber, S.I. Stupp, *Biopolymers (Pept. Sci.)* 94 (2010) 1–18.
- [6] S. Koutsopoulos, L. Kaiser, H.M. Eriksson, S. Zhang, *Chem. Soc. Rev.* 41 (2012) 1721–1728.
- [7] S.E. Paramonov, H.W. Jun, J.D. Hartgerink, *J. Am. Chem. Soc.* 128 (2006) 7291–7298.
- [8] S. Han, S. Cao, Y. Wang, J. Wang, D. Xia, H. Xu, X. Zhao, J.R. Lu, *Chem. Eur. J.* 17 (2011) 13095–13102.
- [9] H. Cui, T. Muraoka, A.G. Cheetham, S.I. Stupp, *Nano Lett.* 9 (2009) 945–951.
- [10] I.A. Nyrkova, A.N. Semenov, A. Aggeli, N. Boden, *Eur. Phys. J. B* 17 (2000) 481–497.
- [11] A. Aggeli, I.A. Nyrkova, M. Bell, R. Harding, L. Carrick, T.C.B. McLeish, A.N. Semenov, N. Boden, *Proc. Natl. Acad. Sci. USA* 98 (2001) 11857–11862.
- [12] H. Cui, A.G. Cheetham, E.T. Pashuck, S.I. Stupp, *J. Am. Chem. Soc.* 136 (2014) 12461–12468.
- [13] Y. Zhao, J. Wang, L. Deng, P. Zhou, S. Wang, Y. Wang, H. Xu, J.R. Lu, *Langmuir* 29 (2013) 13457–13464.
- [14] M.R. Caplan, E.M. Schwartzfarb, S. Zhang, R.D. Kamm, D.A. Lauffenburger, *Biomaterials* 23 (2002) 219–227.
- [15] P. Chen, *Colloids Surf. A* 261 (2005) 3–24.
- [16] Y. Hong, R.L. Legge, S. Zhang, P. Chen, *Biomacromolecules* 4 (2003) 1433–1442.
- [17] N.R. Lee, C.J. Bowerman, B.L. Nilsson, *Biomacromolecules* 14 (2013) 3267–3277.
- [18] D.M. Marini, W. Hwang, D.A. Lauffenburger, S. Zhang, R.D. Kamm, *Nano Lett.* 2 (2002) 295–299.
- [19] G. Colombo, P. Soto, E. Gazit, *Trends Biotechnol.* 25 (2007) 211–218.
- [20] P. Tamamis, L. Adler-Abramovich, M. Reches, K. Marshall, P. Sikorski, L. Serpell, E. Gazit, *G. Archontis, Biophys. J.* 96 (2009) 5020–5029.
- [21] D. Zanuy, Y. Porat, E. Gazit, R. Nussinov, *Structure* 12 (2004) 439–455.
- [22] A.K. Metha, K. Lu, W.S. Childers, Y. Liang, S.N. Dublin, J. Dong, J.P. Snyder, S.V. Pingali, P. Thiagarajan, D. Lynn, *J. Am. Chem. Soc.* 130 (2008) 9829–9835.

- [23] O.-S. Lee, S.I. Stupp, G.C. Schatz, *J. Am. Chem. Soc.* 133 (2011) 3677–3683.
- [24] G. Wei, A.I. Jewett, J.-E. Shea, *Phys. Chem. Chem. Phys.* 12 (2010) 3622–3629.
- [25] C. Liang, P. Derreumaux, G. Wei, *Biophys. J.* 93 (2007) 3353–3362.
- [26] K. Tao, J. Wang, P. Zhou, C. Wang, H. Xu, X. Zhao, J.R. Lu, *Langmuir* 27 (2011) 2723–2730.
- [27] H. Xu, J. Wang, S. Han, J. Wang, D. Yu, H. Zhang, D. Xia, X. Zhao, T.A. Waigh, J.R. Lu, *Langmuir* 25 (2008) 4115–4123.
- [28] M.S. Lamm, K. Rajagopal, J.P. Schneider, D.J. Pochan, *J. Am. Chem. Soc.* 127 (2005) 16692–16700.
- [29] D. van der Spoel, E. Lindahl, B. Hess, G. Groenhof, A.E. Markand, H.J.C. Berendsen, *J. Comput. Chem.* 26 (2005) 1701–1718.
- [30] G.A. Kaminski, R.A. Friesner, J. Tirado-Rives, W.L. Jorgensen, *J. Phys. Chem. B* 105 (2001) 6474–6487.
- [31] A. Onufriev, D. Bashford, D.A. Case, *Proteins* 55 (2004) 383–394.
- [32] H.J.C. Berendsen, J.P.M. Postma, W.F. van Gunsteren, A. Dinola, J.R. Haak, *J. Chem. Phys.* 81 (1984) 3684–3690.
- [33] W.L. Jorgensen, J. Chandrasekhar, J.D. Madura, R.W. Impey, M.L. Klein, *J. Chem. Phys.* 79 (1983) 926–935.
- [34] B. Hess, H. Bekker, H.J.C. Berendsen, J.G.E.M. Fraaije, *J. Comput. Chem.* 18 (1997) 1463–1472.
- [35] T. Darden, D. York, L. Pedersen, *J. Chem. Phys.* 98 (1993) 10089–10092.
- [36] W.G. Hoover, *Phys. Rev. A* 31 (1985) 1695–1697.
- [37] M. Parrinello, A. Rahman, *J. Appl. Phys.* 52 (1981) 7182–7190.
- [38] S. Nosé, M.L. Klein, *Mol. Phys.* 50 (1983) 1055–1076.
- [39] A. De Simone, L. Esposito, C. Pedone, L. Vitagliano, *Biophys. J.* 95 (2008) 1965–1973.
- [40] W. Humphrey, A. Dalke, K. Schulten, *J. Mol. Graph.* 14 (1996) 33–38.
- [41] Discovery Studio Visualizer. Accelrys Inc., San Diego, CA, USA.
- [42] Y. Kallberg, M. Gustafsson, B. Persson, J. Thyberg, J. Johansson, *J. Biol. Chem.* 276 (2001) 12945–12950.
- [43] E. Gazit, *FEBS J.* 272 (2005) 5971–5978.
- [44] M.L. de la Paz, K. Goldie, J. Zurdo, E. Lacroix, C.M. Dobson, A. Hoenger, L. Serrano, *Proc. Natl. Acad. Sci. USA* 99 (2002) 16052–16057.
- [45] C.J. Bowerman, D.M. Ryan, D.A. Nissan, B.L. Nilsson, *Mol. Biosyst.* 5 (2009) 1058–1069.
- [46] A. Aggeli, M. Bell, L.M. Carrick, C.W.G. Fishwick, R. Harding, P.J. Mawer, S.E. Radford, A.E. Strong, N. Boden, *J. Am. Chem. Soc.* 125 (2003) 9619–9628.
- [47] L. Ziserman, H.-Y. Lee, S. Raghavan, A. Mor, D. Danino, *J. Am. Chem. Soc.* 133 (2011) 2511–2517.
- [48] R.L.B. Selinger, J.V. Selinger, A.P. Malanoski, J.M. Schnur, *Phys. Rev. Lett.* 93 (2004) 158103.
- [49] E.T. Pashuck, S.I. Stupp, *J. Am. Chem. Soc.* 132 (2010) 8819–8821.
- [50] T. Muraoka, H. Cui, S.I. Stupp, *J. Am. Chem. Soc.* 130 (2008) 2946–2947.
- [51] H.-Y. Lee, H. Oh, J.-H. Lee, S.R. Raghavan, *J. Am. Chem. Soc.* 134 (2012) 14375–14381.